Chromium removal from contaminated soil using a novel FeO_x/granular activated carbon-based three-dimensional electrokinetic system

Yujie Yan[a,d,e*], Zhang Ling[a], Wen Shu[a], Tao Huang[b, c*], Rich Crane[d,e]

[a] *Engineering Research Center of Biofilm Water Purification and Utilization Technology, Ministry of Education, College of Civil Engineering and Architecture, Anhui University of Technology, Maanshan, Anhui 243002, China*

[b] *School of Materials Engineering, Changshu Institute of Technology, 215500, China*

[c] *School of Chemical Engineering & Technology, China University of Mining and Technology, Xuzhou, Jiangsu, 221116, China*

[d] *Camborne School of Mines, Department of Earth and Environmental Sciences, Penryn Campus, University of Exeter, TR10 9EZ, UK*

[e] *Environment and Sustainability Institute, Penryn Campus, University of Exeter, TR10 9EZ, UK*

* Corresponding authors.

Email addresses: yyj108@ahut.edu.cn (Y. Yan); ht1104705720@qq.com (T. Huang)

Chromium removal from contaminated soil using a novel FeO_x/granular activated carbon-based three-dimensional electrokinetic system

Abstract

A novel three-dimensional electrokinetic remediation (3D EKR) system, with FeO_x/granular activated carbon (GAC) composite constituting a third electrode was investigated for the removal of Cr from a real contaminated soil. Such third electrode particles were distributed evenly throughout the contaminated soil and their additional presence enabled the generation of a higher and more stable current density and reduced acid-base polarization of the soil, when compared against a conventional 2D EKR (cathode-anode) system. This resulted in a higher Cr removal, which was primarily driven by enhanced oxidation of Cr(III) to more mobile Cr(VI) aqueous complexes, which electromigrated towards the anode and into the anolyte. Analysis of FeO_x/GAC and soil samples before and after EKR using XRD, FTIR, SEM-EDS, and XPS confirmed that: (i) both oxidation of Cr(III) and reduction of Cr(VI) occurred simultaneously on particle electrode surfaces; and (ii) aqueous Cr transport governed by electromigration was enhanced by Electro-Fenton reactions and hydrolysis on FeO_x/GAC. A further benefit of 3D EKR was the promotion of residual Cr(III), in proximity to the cathode, to barely soluble crystalline silicate phases, therefore further decreasing the overall toxicity of the soil. This study therefore provides a highly promising first insight into the use of 3D EKR for the removal of Cr from contaminated land. Future work will seek to examine this emerging new technology at large scale and for different contaminated land scenarios, therefore further developing it towards a potential commercial application.

Keywords: Chromium, Particle electrode, Electro-Fenton, 3D electrokinetics, soil remediation

Graphical Abstract

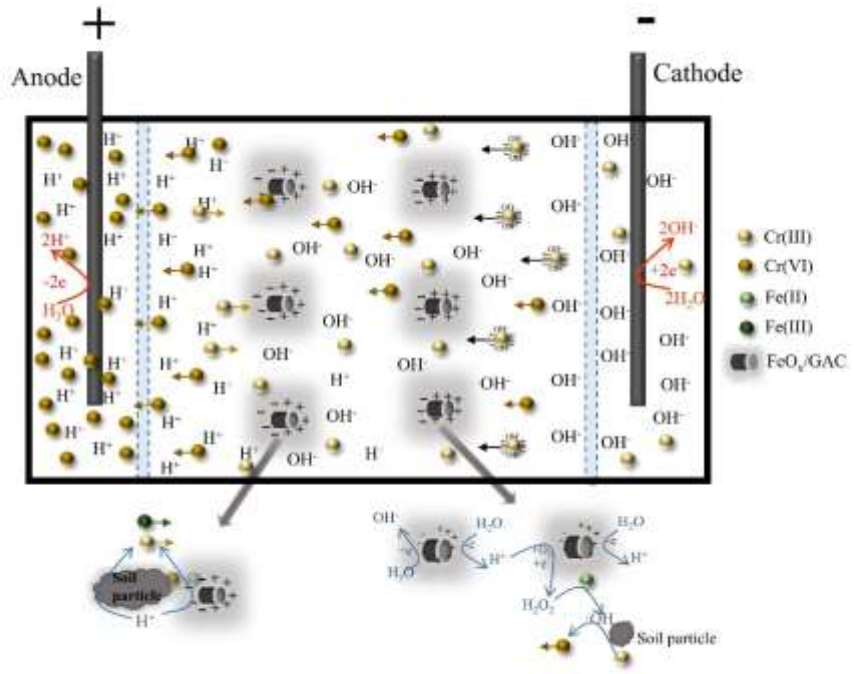

1. Introduction

Chromium (Cr), is a common industrial feedstock and used in a wide range of processes, including: electroplating, alloy manufacturing, leather processing and ceramic production[1,2]. Consequently, large quantities of Cr-bearing wastewaters and residues are produced each year and legacy sites containing Cr at elevated concentrations are numerous[3,4]. The most common and stable valence of Cr in soils are trivalent (Cr(III)), typically in the form of hydroxides and oxides, and hexavalent (Cr(VI)), typically as $HCrO_4^-$, CrO_4^{2-} or $Cr_2O_7^{2-}$. The latter valence state is considered significantly more problematic due to its carcinogenic and genotoxic properties[5]. Furthermore the often high solubility and associated mobility exhibited by Cr(VI) in soils can lead to pollution over wide areas[6], impacting plant, animal and human receptors[7,8].

Conventional technologies used to remediate Cr-contaminated soils include phytoremediation[9], soil washing[10,11], and immobilization[12]. Such methods can be effective under certain scenarios, however, disadvantages include the generation of secondary pollution, incomplete metal removal, and high reagent consumption[13–15]. Amongst the alternative techniques currently available, electrokinetic remediation (EKR) has emerged as highly promising due to its high efficacy for such contaminant metal removal combined with its ability to be applied in-situ and thereby circumvent the high cost and environmental/human hazard associated with contaminated land excavation[16,17]. The principle of EKR is to apply an electric potential between a pair, or array, or electrodes which are distributed laterally across a contaminated site, in order to enable the electromigration of target pollutants towards either the anode or the cathode, depending on the nature of their charge[18,19]. Within this scheme, the following mechanisms are typically exploited in order to enable Cr removal: (1) Cr(VI), present as a soluble oxyanion, is transported via electromigration into the anolyte[20]; (2) Cr(III), present as a soluble cation, is transported via electromigration into the catholyte; and/or (3) Cr(VI) undergoes chemical reduction to Cr(III) wherein it becomes sorbed and/or precipitated within the soil matrix[21]. Given the fact that such processes are intrinsically dependent on multiple electrochemical factors, including: the redox and pH gradient, presence or absence of competing ions and solution ionic strength, their precise control is vitally important in order to

ensure high performance of the EKR process. For example, during EKR H^+ and OH^- ions are generated on the anode and cathode respectively (Eqs. (1) and (2)) which can then electromigrate into the contaminated soil, affecting the soil pH and subsequently the fate and mobility of Cr[22,23]. Therefore, effective pH control is amongst the most vital considerations in determining an effective strategy for EKR application for Cr removal[3]. Current approaches to control pH include buffer solution injection, use of ion-exchange membranes, electrode switching, approaching anode technique, and electrolyte recirculation[24–27].

In recent years a new concept has been explored, which comprises the incorporation of three-dimensional (3D) electrodes within the EKR process. Research remains in its infancy, however, preliminary results suggest that it has the potential to unlock new paradigms for metal removal efficacy[3,28]. The technique comprises the dissemination of conductive particles, such as activated carbon, graphite, metallic particles, modified kaolin or carbon aerogels, throughout the soil matrix, in order for them to become polarized by the external voltage and thereby form an array of charged microelectrodes; one side of each particle comprising an anode, the other a cathode[29]. This can both improve the efficacy of the EKR process via the overall lowering of the resistivity of the soil media, but can also enable stronger buffering of solution pH due to enhanced water electrolysis and mass transfer processes[3].

$$\text{Anode: } H_2O \rightarrow 2H^+ + {}^1/_2\, O_2\,(g) + 2e^- \quad (1)$$

$$\text{Cathode: } 2H_2O + 2e^- \rightarrow 2OH^- + H_2\,(g) \quad (2)$$

In addition, such particle electrodes, play multiple roles in a range of further electrochemical processes, including contaminant metal adsorption/electrosorption, oxidation/electrocatalytic degradation, and electrocoagulation. Prudent application of both 3D EKR electrode media composition and application conditions can therefore result in a major improvement in contaminant removal compared to conventional two-dimensional (2D) EKR. For Cr-contaminated soil remediation, reduction of Cr(VI) to insoluble Cr(III) is a widely accepted strategy, and many lab-scale experiments of EKR-driven Cr(VI) reduction have been reported[30–32]. Whilst such Cr precipitation can result in the immobilization of Cr (a pH and

redox (Eh) electrochemical window of 3＜pH＜7 and -200 mV ＜Eh＜500 mV is typically targeted in order to enable the formation of $Cr(OH)_3$, which exhibits low solubility) and therefore lowers the ecotoxicity that the contaminated land poses[33], such residual Cr(III) is known to undergo oxidation back to Cr(VI), e.g. by reaction with manganese oxides[34]. It is therefore clear that removal of total Cr (i.e., both trivalent and hexavalent forms) is preferred. Given that Cr(VI) is typically soluble and can exhibit enhanced mobility under EKR it is proposed herein that oxidation of Cr(III) to Cr(VI) could represent an effective strategy for total removal of Cr from the soil. Whilst such a scheme is counterintuitive from an environmental protection perspective, due to the need to temporarily increase the ecotoxicity that such Cr would pose, if implemented correctly, and all such Cr is extracted from the soil and collected in a target electrode reservoir (or via direct electrodeposition onto the electrode), then it would indeed represent the most appropriate methodology.

The oxidation of Cr(III) to Cr(VI) in an EKR system can be achieved by the generation of strong oxidants, namely: hydroxyl radicals (·OH), which can be identified by techniques including electron paramagnetic resonance (EPR)[35], quenching methods[36,37], and UV/fluorescence probe method[38,39].Many studies have confirmed that the concentration of ·OH in a 3D EKR system can be significantly higher than in conventional 2D EKR systems[40]. Within such 3D EKR systems activated carbon (AC) is often applied due to its ability to act as a high surface area site for heterogeneous catalysis reactions[41,42]. Studies on composite iron oxides as catalyst on efficient adsorption removal or EK removal of Cr have been widely reported[43–45]. The coupling of AC with iron-bearing media affords the further benefit of inducing electro-Fenton (E-Fenton) reactions (Eqs. (3) - (5))[29], which has the potential to unlock new advances in how we can efficiently generate ·OH[46]. Especially, it was reported the mixed valence iron oxides containing both Fe(II) and Fe(III) showed higher catalytic activity than conventional single valence iron oxide regarding E-Fenton system[46,47]. Thus, the potential merits of 3D EKR using iron (oxides)-loaded AC composite as the third electrode are numerous and include: enhanced pH control, mass transfer, and generation of oxidants.

$$O_2 + 2H^+ + 2e^- \rightarrow H_2O_2 \quad (3)$$

$$H_2O_2 + Fe^{2+} \rightarrow Fe^{3+} + OH^- + \cdot OH \quad (4)$$

$$Fe^{3+} + e^- \rightarrow Fe^{2+} \quad (5)$$

Research on the use of such composite particles within 3D EKR for soils remain almost entirely unexplored. This study has therefore been established in order to bridge this gap in our understanding and apply this novel 3D EKR system for the remediation of Cr from a real contaminated soil sample. Specific aims of this study include: (1) the synthesis of a 3D EKR particle electrode which is low cost but also possesses highly favorable properties as a heterogeneous E-Fenton catalyst. For this purpose, granular activated carbon (GAC) made from coconut shell was selected. Such carrier particles were then loaded with mixed valance iron oxide particles, comprising hematite and magnetite. (2) Investigate the application of such a FeO_x/GAC 3D EKR system for the removal of Cr from a real contaminated site. For this purpose contaminated soil has been selected from an abandoned chromium salt production plant in Chongqing, China. Given the aforementioned ·OH detection methods are associated with the addition of organic spin traps or scavengers[48] and is not practical to be incorporated with the static 3D EKR setup for the soil system, the possible effect of E-Fenton reaction was indirectly elucidated by the occurrence and chemistry of Cr and Fe in both solid and aqueous before and after 3D EKR application, using a range of analytical techniques. Overall this work has therefore been established in order to further examine the suitability of 3D EKR process as a potentially highly effective new tool for Cr remediation from currently difficult to treat contaminated soil.

2. Experimental

2.1 Chemicals and materials

Deionized (DI) water (resistivity >18.2 MΩ cm) was used in all solutions and experiments. All chemicals used were analytical grade (ferrous sulfate ($FeSO_4 \cdot 7H_2O$), citric acid ($C_6H_8O_7$), sodium sulfate (Na_2SO_4), sodium hydroxide (NaOH), potassium chloride (KCl), and nitric acid (HNO_3)) and purchased from Aladdin Co., China. Coconut shell-derived GAC (purchased from

Henan lvlin Activated carbon Co., Ltd, China) was purified by magnetic stirring in DI water for 2 h, after which it was rinsed until there was no ash in the rinsed water, and then dried at 105 °C overnight. Cr-contaminated soil was collected from an abandoned chromium salt production plant in Chongqing, China. The sample was dried at 105 °C overnight, sifted through a 100-mesh sieve (hereinafter as original soil sample), and sealed in the polyethylene bucket at room temperature until the EKR experiments were carried out.

2.2 Synthesis and characterization techniques of FeO_x/GAC

The mixed-valance iron oxide particle electrodes FeO_x/GAC were synthesized through the impregnation-calcination method[49], illustrated in **Fig. S1** in Supplementary Material (**SM**). Different batches were prepared under a range of conditions, i.e., solid to liquid (S/L, 1:0 - 1:4) ratio, calcination time (1 - 3 h), and temperature (200 - 600 °C), more details are included in **Table S1** in **SM**. A given mass of pretreated GAC (**Table S1**) was first immersed in 0.4 M $FeSO_4$ solution, and the solid-liquid mixture was then sealed and shaken in a horizontal oscillator at 25 °C for 10 h. The solid product was then filtrated, using a 0.45μm nylon filter, and dried at 105 °C for 2 h in an N_2 atmosphere. The dried product was then calcined in a tube furnace at a given temperature for a given time (**Table S1**) in the presence of N_2 to enable the loading of iron oxides onto the GAC surface. The resultant FeO_x/GAC products were then each held under vacuum ($<10^{-4}$ mbar) until being used for EKR experiments.

The surface area and pore sizes of GAC and FeO_x/GAC were detected by N_2 adsorption-desorption isotherm at 77 K after heat treatment under vacuum at 573 K for 3 h (BET, max-II, MicrotracBEL). The X-ray diffraction (XRD) patterns were obtained on a X' Pert Powder diffractometer with Cu K_α at 45 kV and 55 mA over the 2θ range 5º - 90º. The functional group structure of GAC and FeO_x/GAC was performed by fourier transform infrared spectroscopy (FTIR, Nicolet iS50, Thermo). The surface morphology and elemental analysis was measured using a scanning electron microscope (SEM, TM4000Plus II, Hitachi) equipped with energy-dispersive spectroscopy (EDS). Surface-sensitive elemental composition and valence state of Cr was measured using X-ray photoelectron spectroscopy (XPS, ESCALAB 250Xi, Thermo).

2.3 Electrokinetic experiments

EKR experiments were conducted using a rectangular polymethyl methacrylate reactor, as shown in **Fig. 1**. The reactor (L=20 cm, W=6 cm, H=8 cm) was divided into three compartments: the anode chamber, the soil remediation chamber, and the cathode chamber. The anode chamber was used to house a graphite plate (L=6 cm, W=6 cm) and the anolyte, and the cathode chamber was used to house a stainless-steel plate (L=8 cm, W=6 cm) and the catholyte. The counter electrodes are connected to a DC power supply (Longwei, LW-K603D) through seven strands of aluminum wire, with an outer diameter of 6.7 mm. The three compartments are separated by two 100 μm aperture nylon-covered plexiglass grids, located 2 cm from each counter electrode.

Three groups of 3D EKR experiments were performed (**Table 1**). In Group A, 3D EKR experiments using 24 different types of FeO_x/GACs (synthesized under a range of different S/L ratios, temperatures and calcination times; see **Table S2** in **SM** for further detail) were analyzed, each with a remediation time of 3 d. The FeO_x/GAC used in Groups B (No. 25-27) and C (No.28-30) was optimized based on the range analysis and variance analysis from Group A. During each EKR, 7.5 g synthesized FeO_x/GAC was thoroughly mixed with 150 g Cr-contaminated soil and DI water in order to ensure full saturation. The mixture was then packed in the soil remediation chamber. The initial anolyte and catholyte were 250 mL of 0.1 M Na_2SO_4. The soil remediation chamber was divided into 5 Sections: I, II, III, IV, and V from near anode to near cathode. The pH, electric conductivity (EC) of Sections I-V, and current density were measured every 12 h during experiments. All experiments were conducted under the constant voltage gradient of 1V/cm. At the end of each experiment, the soil Sections were each excavated and dried in an oven at 105 °C overnight (labeled with experiment No.-section No, e.g., 1-I, 2-II). The used FeO_x/GAC was separated from each section and each stored in a sealed plastic bag. The generated liquid waste in anode chamber and cathode chamber was collected and labelled properly in polytetrafluoroethylene (PTFE) containers for disposal.

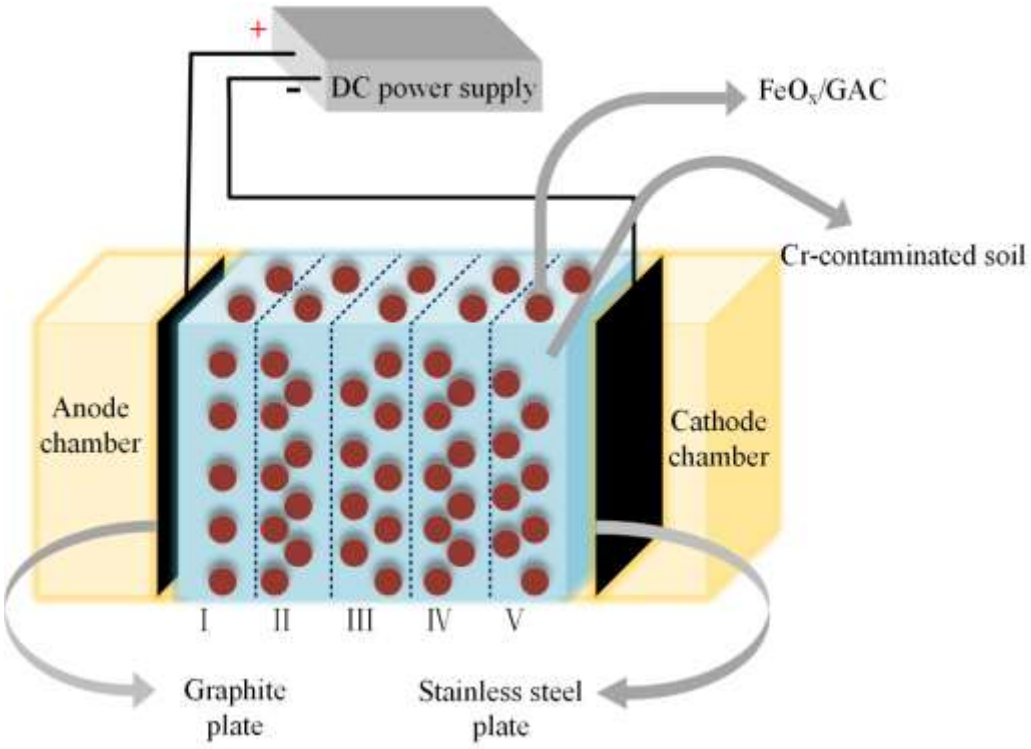

Fig. 1 The apparatus for EKR experiments

Table 1. Arrangement of (3D) EKR experiments

Treatment group	Experiment No.	Duration (d)	Add to soil	Evaluating index
Group A	1-24	3	FeO_x/GAC	Cr leaching conc.
Group B	25	5	--	Cr conc. and leaching
	26	5	GAC	Cr conc. and leaching
	27	5	FeO_x/GAC*	Cr conc. and leaching
Group C	28	7	FeO_x/GAC*	Cr leaching
	29	10	FeO_x/GAC*	Cr leaching
	30	13	FeO_x/GAC*	Cr leaching

* Represents the optimized particle electrode from group A

2.4 Analytical methods

The soil pH was measured in the suspension of dry soil and 1 M KCl at a ratio of 1:2.5 using a pH meter (PHS-3C, Rex, China). The soil EC was measured using a conductivity meter (DDSJ-308A, Rex, China) by suspending 10.0 g of dry soil in 25 mL DI water after 30 min

shaking. The soil Eh was measured directly using a portable Eh meter (SX731, Sanxin, China). Organic matter content was determined by ignition loss after 1 h at 550 °C. Carbonate content was determined using the Scheibler method and the calculation was based on the standard curve of calcium carbonate. The cation exchange capacity (CEC) was determined using ammonium-acetate method[50]. Water content was calculated according to the mass difference before and after drying 5 g of fresh soil at 105 °C for 16 h. The concentration of total Cr in soil was measured by Flame atomic absorption spectrometry (AAS, AA-6300C, Shimadzu) after acid digestion according to EPA Method 3050B. The Cr(VI) concentration in soil was determined by ultraviolet spectrophotometer (UV-2100, Japan) after alkaline digestion according to EPA Method 3060A. Cr(III) was therefore determined using mass balance. The leaching concentration of Cr(VI) and total Cr in soil was determined by the sulphuric acid & nitric acid method (HJ/T299-2007, China), with analysis by UV spectrophotometry (UV-2100, Japan) and inductively coupled plasma-optical emission spectrometry (ICP-OES, iCAP 6300 Duo), respectively. All measurements were performed in triplicate except for the real-time measurement of current density and soil pH as a function of time. The elemental composition and mineral phase in the original soil was confirmed by X-ray fluorescence (XRF, XRF-1800, Shimadzu) and X-ray diffraction (XRD, X'Pert Powder), respectively.

2.5 Calculations

The removal efficiency of Cr(VI), total Cr, Cr(VI) leaching, and total Cr leaching was calculated as follows:

$$\mathrm{Y} = (C_0 - C_i)/C_0 \times 100\% \quad (6)$$

Where Y is the removal efficiency (%), C_0 is the initial concentration (mg/kg or mg/L), C_i is the concentration (mg/kg or mg/L) in soil region i after EKR treatment.

The average removal efficiency was defined as the mean of five sections (I-V), calculated as follows:

$$\mathrm{y} = \frac{\sum_{i=1}^{5} \frac{C_i - C_0}{C_0}}{5} \times 100\% \quad (7)$$

Where y is the average removal efficiency (%), C_0 is the initial concentration (mg/kg or mg/L), C_i is the concentration (mg/kg or mg/L) in soil section i after EKR treatment.

3. Results and discussion

3.1 Soil characterization

Some characteristics of the Cr contaminated soil are given in **Table 2** and **Fig. 2**. No specific structure or morphology was observed. Particle size was predominantly within the range of 2-200 μm and therefore classified as a loam. An average pH value of 8.19 was recorded. This alkalinity could be derived from hydrolysis of the Cr residue's calcium and magnesium mineral phases. The CEC is relatively low (7.18 - 10.02 cmol/kg), which can be due to the occupation of the colloidal adsorption sites by Cr(III) in the soil. The soil EC and water contents are 51.88 mS/cm and 16.53%, respectively. The Eh is quite low, indicating the high content of reduced substances in the soil. The main components of the soil, determined by XRF, are Ca, O, Si, Al, Cr, Fe, and Mg. The high Ca content (13.32%) was likely to be due to the high-calcium roasting process of the Cr-salt production at the contaminated site. The Cr content (9.12%) is much higher than the typical background value of Cr content in non-contaminated soil. The concentration of Cr(VI) and Cr(III) was 520.79 mg/kg and 14298.68 mg/kg, respectively, far exceeding the control value (78 mg/kg) of Cr(VI) for industrial land use (GB36600-2018). The leaching concentration of Cr(VI) and total Cr are 15.95 mg/L and 32.9 mg/L, respectively, exceeding the limiting values of leaching toxicity for hazardous wastes (GB5085.3-2007), which poses a potential risk to the environment. The Cr-containing crystalline phase was not detected using XRD in the original soil (Fig. 2d), indicating that Cr was amorphous prior to EKR remediation. The existence of hexagonal rhombohedral crystal calcite (Calcite, $CaCO_3$, PDF# 05-0586) and orthorhombic crystal aragonite (Aragonite, $CaCO_3$, PDF# 41-1475) indicated the high content of magnesium ions and carbonate[51], which is consistent with the XRF result of the original soil in Fig. 2c.

Table 2. Physiochemical characteristics and Cr content in the original soil sample

Properties	Value	Limiting value (national standard)

pH	8.19 ± 0.07	--
EC (mS/cm)	51.88 ± 0.86	--
CEC (cmol/kg)	8.52 ± 1.31	--
Eh (mV)	-121 ± 9.46	--
Organic matter (g/kg)	15.15 ± 2.56	--
Water content (%)	16.53 ± 1.18	--
Saturated moisture (%)	70.2 ± 0.93	--
Cr(VI) conc. (mg/kg)	520.79 ± 7.03	78 (GB36600-2018)
Total Cr conc.(mg/kg)	14298.68 ± 1083.38	--
Leaching conc. of Cr(VI) (mg/L)	15.95 ± 1.90	5.0 (GB 5085.3-2007)
Leaching conc. of total Cr (mg/L)	32.90 ± 4.62	15.0 (GB 5085.3-2007)

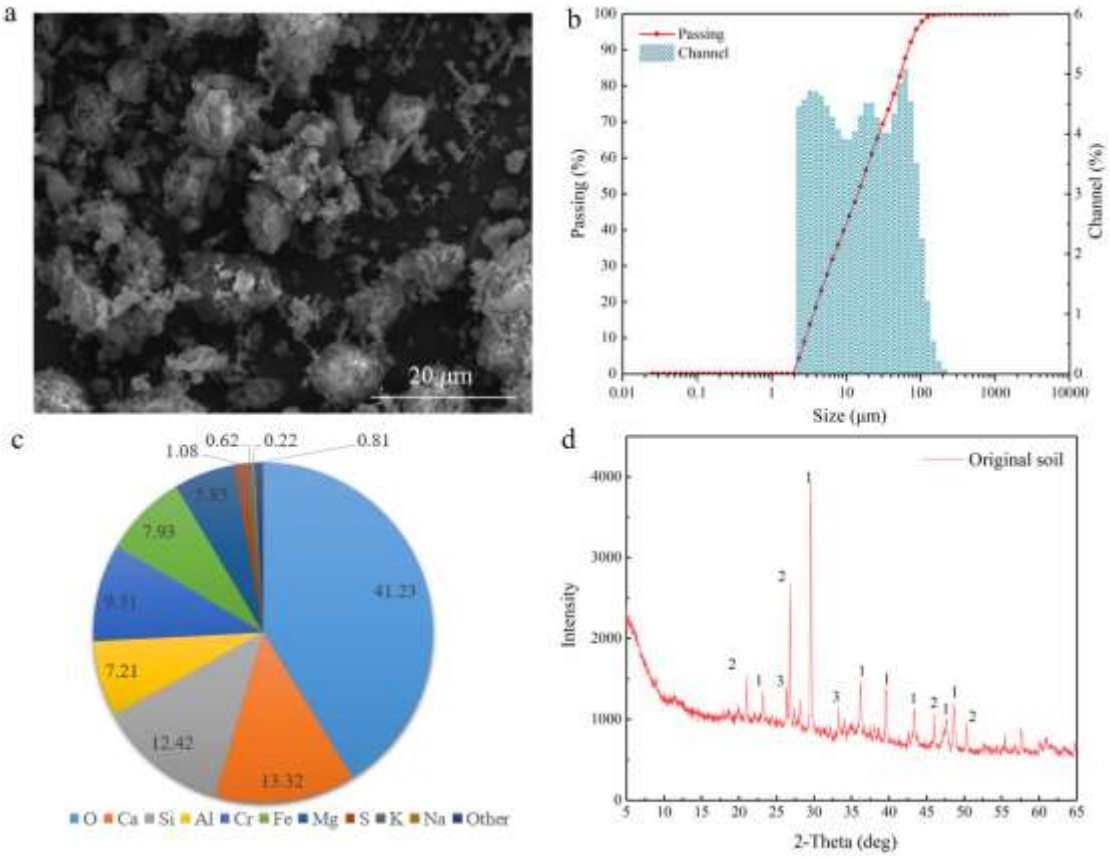

Fig 2. Original soil characteristics: (a) SEM images, (b) particle size distribution, (c) elemental component, and (d) XRD pattern. 1: Calcite, $CaCO_3$; 2: Quartz, SiO_2; 3: Aragonite,

$CaCO_3$

3.2 Optimization of FeO_x/GAC

Different types of FeO_x/GAC particle electrodes, each synthesized under different conditions (**Table S2**), were applied for the 3 d EKR remediation. The impact of the three different synthesis variables (calcination time, S/L, and calcination temperature) on the removal efficiency of Cr(VI) leaching in EKR are shown in **Fig. 3**, along with the k value in range analysis. It can be seen in **Fig. 3a** that the removal of Cr(VI) leaching increased with the increasing calcination time, reaching a peak at 2 h, before decreasing. During this initial calcination process, the decomposition of $FeSO_4$ to Fe_3O_4 occurred. As it continued over 2 h, it is likely that this high-temperature heat treatment resulted in damage to the pore structure of the GAC (lowering of surface area)[52]. This may decrease the adsorption sites on the particle electrode and thus influence the reduction and adsorption of Cr(VI) by particle electrodes during EKR. The S/L ratio significantly affected the removal of Cr(VI) leaching (**Fig. 3b**). At a S/L ratio of 1:0 no $FeSO_4$ (and therefore no iron oxide) was present and as such the efficacy of Cr(VI) removal using 3D EKR was low. As the S/L ratio was increased towards 1:3 the efficacy of Cr(VI) removal using 3D EKR increased, which is attributed to the increased loading of $FeSO_4$ onto the GAC surface. At such concentrations loading of $FeSO_4$ onto GAC was considered to comprise less than a monolayer, wherein the subsequent conversion of $FeSO_4$ into iron oxides we observed to form within the inner surface of the GAC, in an amorphous state[53]. In this case, the particle electrodes could now both reduce and absorb the Cr(VI), which contributed to an increase in Cr(VI) removal efficacy. When the S/L ratio increased to 1:4, however, the black iron oxide product crystals were observed to also adhere to the crucible. This is attributed to the high amount of $FeSO_4$, possibly forming a total monolayer[54], and thereby allowing little exposure of the GAC to the Cr(VI) during the 3D EKR process.

The calcination temperature had a considerable effect on the removal of Cr(VI) (**Fig. 3c**). $FeSO_4$ cannot be fully decomposed to iron oxides at low temperature, resulting in insufficient modification of GAC, which in turn affected its ability to both sorb and chemically reduce the

Cr(VI) during the 3D EKR process. At high temperatures (500 - 600 °C), the GAC can be ablated, resulting in a decrease in surface area and porosity. Its ability to retain iron oxide products was therefore decreased, which in turn caused a decrease in its performance for Cr(VI) removal using 3D EKR.

Based on these aforementioned results, a series of orthogonal experiments were designed to optimize the synthesis of FeO_x/GAC. The L9 (3^3) orthogonal design and results regarding removal efficiency of Cr(VI) leaching are shown in **Table S2** in the **SM**. The three factors A, B, and C, represents the calcination time, S/L, and calcination, respectively. The range analysis and variance analysis of the orthogonal experiment is given in **Table S3** in the **SM**. The influence of factors in different levels on removal efficiency of Cr(VI) leaching is illustrated in **Fig. 3d** based on range analysis. The influence degree of factors A, B, and C on the removal of Cr(VI) leaching was interpreted to be B>C>A, and the optimum process conditions to be S/L of 1:3, calcination temperature of 350 °C , and calcination time of 2 h. The particle electrodes are hereinafter referred to as the FeO_x/GAC particles prepared under the optimum conditions.

The characterization of FeO_x/GAC is illustrated in **Fig. 4**. The particle electrodes retained the skeleton and pore structure which is typical of raw GAC, and the particle surface was evenly covered with a large number of hexagonal flake-like crystals of uniform size (**Fig. 4a** and **4b**). A slight agglomeration of the particles was also observed. The main components of crystals were analyzed to be O and Fe (**Fig. 4c**). Results from XRD analysis (**Fig. 4d**) showed the two new peaks of FeO_x/GAC at 2θ=30º and 35º agree with maghemite-C (JCPDS card 39-1346) and magnetite ((JCPDS card 19-0629). Furthermore, the XPS spectra of the core level of Fe $2p_{3/2}$ and O 1s given in **Fig. 4e** indicated the existence of Fe(III), Fe(II), and lattice oxygen[55]. Consequently, the load of Fe_3O_4 and Fe_2O_3 on GAC was confirmed. FTIR spectra of particle electrodes were further characterized to verify the surface functional groups (**Fig. 4f**). The synthesized FeO_x/GAC retained the same stretching vibration of -CHO, -OH, and -C=O as raw GAC. Besides, the FTIR spectrum of the FeO_x/GAC displayed new peaks at 3159 cm^{-1} and 1070 cm^{-1}, attributed to the stretching vibration of -CH and COOH. The presence of the hydroxyl and carboxyl functional groups enhanced the non-polarity of the particle electrode

surface and showed stronger adsorption on Cr[56]. Additionally, peaks attributed to the stretching vibration of Fe-O at 734 cm^{-1} were identified[57], which is consistent with the O 1s analysis of FeO_x/GAC. Further characterization of the electrode particles on N_2 adsorption-desorption isotherms and pore diameter distribution is illustrated in **Fig. S2** in the **SM**.

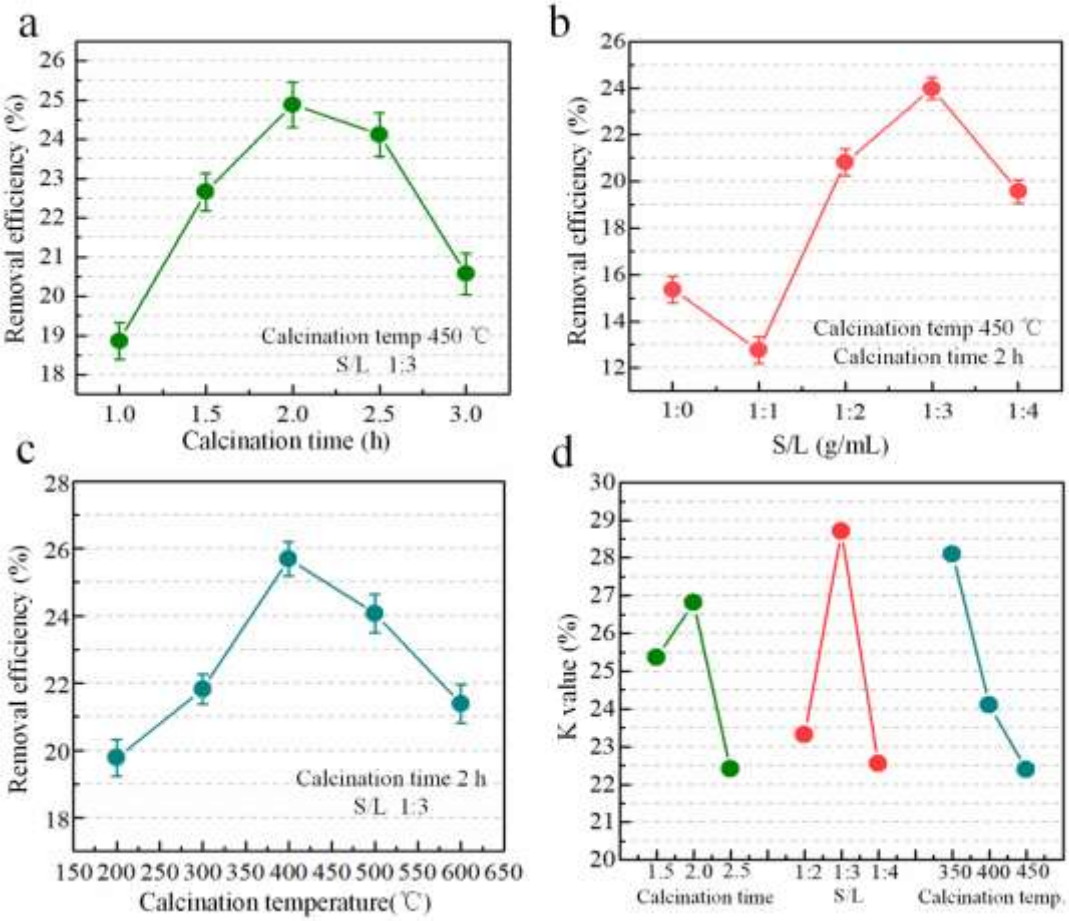

Fig. 3 Effect of different variables employed during FeO_x/GAC electrode particle synthesis on resultant 3D EKR removal efficiency of Cr(VI) leaching: (a) calcination time, (b) S/L ratio, (c) calcination temperature, and (d) k value of different variables in different levels based on range analysis

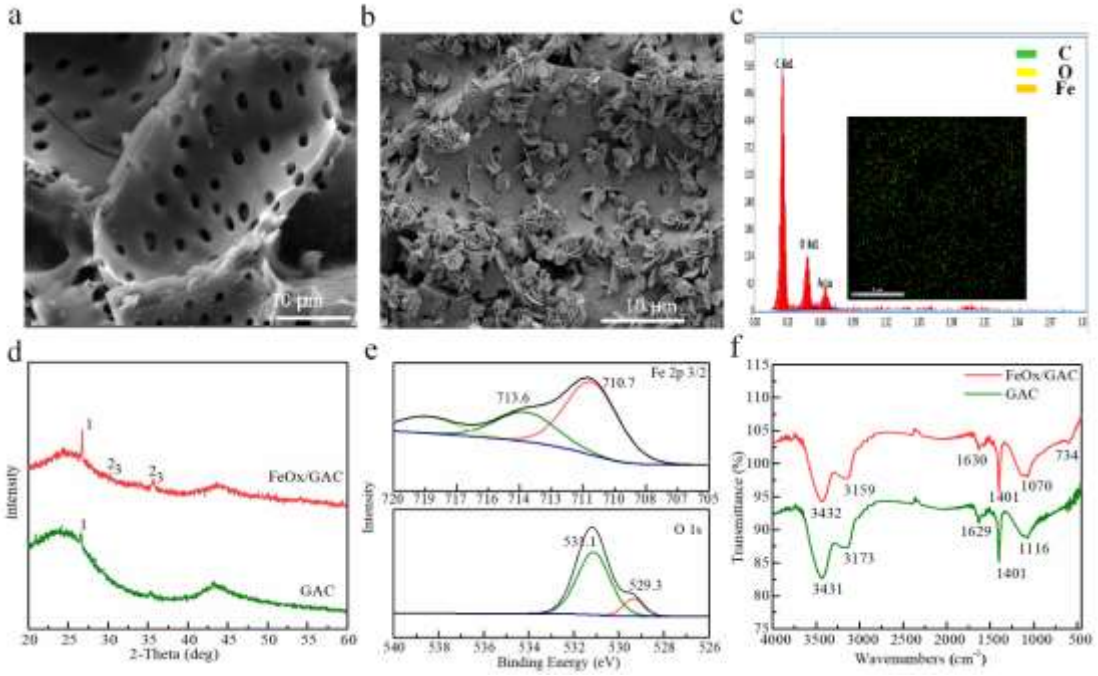

Fig. 4 Characterization of FeO_x/GAC: (a) SEM of raw GAC, (b) SEM of optimized FeO_x/GAC, (c) EDS analysis of FeO_x/GAC, (d) XRD patterns of raw GAC and FeO_x/GAC, (e) high-resolution XPS spectra analysis of Fe $2p_{3/2}$ and O 1s of FeO_x/GAC, and (f) FTIR spectrum of raw GAC and FeO_x/GAC

1: Carbon, C; 2: Maghemite-C, syn, Fe_2O_3; 3: Magnetite, syn, Fe_3O_4

3.3 Changes in pH, EC, and current density

The pH, EC and electrical current are often the important electrokinetic indicators that reflect the electrochemical reactions, physiochemical reactions, and transport of target ions in the EKR system. The **Fig. 5** depicts the trend of changes in soil pH, EC, and current density over time in experiment Group B with a variable of the particle electrode (none, GAC, and FeO_x/GAC). In **Fig. 5a**, the current density exhibited the same tendency, i.e., increasing first and then decreasing, despite of different particle electrodes, which was explained by the law of dissolution and electromigration of mobile ions during EKR. In the case of 2D EKR (i.e., no FeO_x/GAC), the current density (**Fig. 5a**) initiated from 1.66 mA/cm^2 and reached the maximum of 2.89 mA/cm^2 after 24 h. This was slower than the 3D-GAC and 3D-FeO_x/GAC systems which reached their maximum of 2.93 mA/cm^2 and 2.91 mA/cm^2 only after only 12 h, respectively. This was attributed to the bipolar microelectrodes formed in the 3D EKR system,

which enabled the expansion of electrode reactions from the two plate electrodes to the particle electrodes[58]. As a result, the current carriers (mobile ions) in 3D EKR were higher than in the 2D EKR. In addition, free electrons inside the particle electrode also functioned as the carriers, which explained a higher stable current density in 3D-GAC and 3D-FeO_x/GAC throughout 60 - 108 h. In **Fig. 5b**, pH distribution in Group B showed that the acidification (pH 7.82 - 4.01) was mainly observed in Sections I and II, while the alkalization (pH 7.89 - 12.98) mainly observed in Sections III, IV, and V. This was explained by the migration of H^+ and OH^-, produced by electrolysis on the anode and cathode. Interestingly, the pH change rate over time was always lower in 3D experiments, implying a relatively slow acidification/alkalization process. Generally, the acidic environment resulted in the adsorption and accumulation of Cr(VI) oxyanions, and the alkaline soil resulted in the precipitation of Cr(III)[59], which explained the high EC in near anode sections and the low EC in near cathode sections in Group B, as shown in **Fig. 5c**. Noticeably, compared to the 2D experiment, the 3D experiments with GAC and FeO_x/GAC had significant lower EC in Section I and II yet higher EC in Section IV and V. This indicated the less accumulation of Cr(VI) and less precipitation of Cr(III) was achieved simultaneously under 3D EKR.

Fig. 6 shows the time-space scatter of soil pH and conductivity with FeO_x/GAC as the third electrode. The soil pH distribution within each experiment showed the same regularity of increasing from near anode section to near cathode section (Fig. 6a). At the end of experiments after 5, 7, 10, and 13 d remediation, soil pH in Section I decreased to 6.0, 6.9, 4.9, and 4.1, while soil pH in Section V increased to 12.3, 12.7, 12.8, and 11.3, respectively. Particularly, Section I after 13 d remediation was strongly acidic, which enhanced the affinity between Cr(VI) and positively charged inorganic colloids in the soil, resulting in a low removal of Cr(VI). The acidification of soil was expected to expand towards the cathode with the extension of remediation of time due to generation and migration of H^+ in anode. However, acidification in Sections III, IV, and V was not achieved even after 13 d remediation, indicating a considerable OH^- was concentrated in the 3D EKR system. This can be due to the E-Fenton-like reactions (Eqs. (3) and (4)) during which the H^+ was consumed and accompanied by the

generation of OH^-. These three sections were measured as alkaline all the time, which was conducive to the stable migration of Cr(VI). The overall conductivity in Group C was expected to decrease with prolonging of time due to the migration of soluble ions out the soil. However, Fig. 6b indicated an irregular distribution of conductivity over time. Given that the external EK conditions were the same, this irregularity may be attributed to the FeO_x/GAC, which behaved as the bipolar third electrodes, resulting in the generation of H^+ and OH^- and interfere with the spices and migration of soluble ions during EKR process[58].

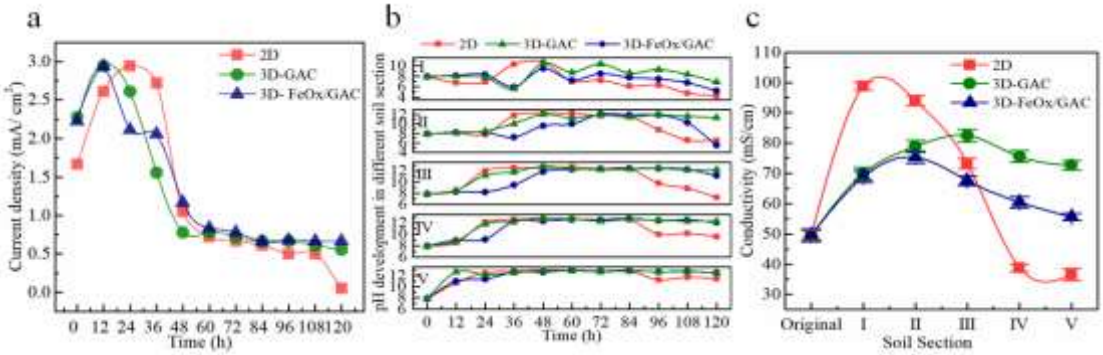

Fig. 5. Effects of the particle electrode on the (a) system current density, (b) soil pH, and (c) soil conductivity in experimental Group B.

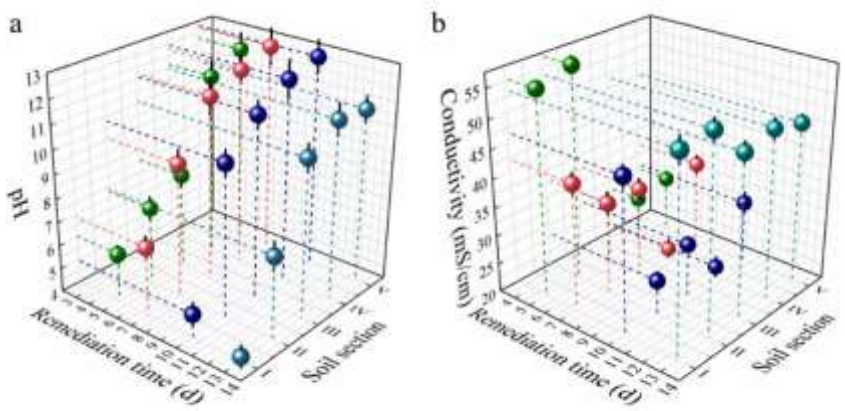

Fig. 6. Effect of the remediation time on the (a) soil pH and (b) conductivity with FeO_x/GAC as the third electrode in experimental Group C.

3.4 Cr concentration and leaching toxicity

Fig. 7 illustrates the distribution of Cr(VI) and total Cr after EKR, along with the removal efficiency of Cr leaching. The distribution of Cr(VI) after remediation showed a typical

polarization phenomenon in the 2D EKR, i.e., lower removal rate in the near anode section (namely Section I, 27.86%) and higher removal rate in the near cathode section (namely Section V, 64.09%), as shown in **Fig. 7a**. Noticeably, Section III had the lowest removal efficiency, which can be explained by the pH jump between Section II (7.82) and Section III (11.94) after 24 h (**Fig. 5b**). This resulted in the precipitation of calcium ions and magnesium ions and formed a focusing band (dead zone)[60], which hindered the migration of CrO_4^{2-}/$HCrO^-$ and therefore resulted in significant accumulation of Cr(VI). This uneven distribution of Cr(VI) reduced the average removal efficiency of the 2D EKR system, which was calculated to be 42.49%. In contrast the average removal efficiency of Cr(VI) was calculated to be 49.24% and 50.09% in 3D-GAC and 3D-FeO_x/GAC, respectively. This improvement was attributed to the additional presence of the third electrodes, i.e., the presence of such particle electrodes can provide a favorable environment for the migration of Cr(VI) due to the fact that such systems exhibit a lower pH increase (and therefore lower tendency to reduce the focusing phenomenon caused by pH jump), and enhance the overall removal of Cr(VI). For the removal of total Cr using either 2D or 3D EKR depends on the migration properties of both Cr(III) and Cr(VI). Namely Cr(VI) oxyanions are known to be able to migrate under both acidic and alkaline conditions, whilst Cr(III) is more sensitive to pH changes and within this has a strong tendency to precipitate in soil under alkaline conditions[61]. Given the fact that Sections III-V were alkaline throughout the experiment and therefore hindered the migration and removal of Cr(III) from the acidic Sections I and II, the total Cr removal was greatly dependent on the removal of Cr(VI). The Cr(VI) comprised 3.6% proportion of total Cr in the original soil (prior to EKR), nevertheless, the average removal efficiency of total Cr reached 23.32% in 3D-FeO_x/GAC remediation, which indicated that a considerable amount of Cr(III) was oxidized into Cr(VI).

Table 3. Removal efficiency recorded from experiment Group B

Group B	Removal efficiency of Cr(VI) (%)			Removal efficiency of total Cr (%)		
	Maximum	Minimum	Average	Maximum	Minimum	Average
2D electrode	64.90 (V)	12.27 (III)	42.48	24.24 (I)	1.77 (II)	8.54

3D -GAC	56.07 (IV)	39.80 (I)	49.29	27.33 (III)	2.49 (V)	19.52
3D -FeO_x/GAC	59.41 (V)	39.09 (I)	50.08	38.66 (II)	1.47 (IV)	23.32

Fig. 7b shows the leaching concentration of Cr(VI) in different soil sections after EKR treatment. The overall leaching concentration of Cr(VI) was still high after the 2D EKR treatment, which was 8.39, 8.45, 8.77, 3.77, and 6.15 mg/L from Section I to Section V, respectively. In 3D FeO_x/GAC EKR, the leaching concentration in Sections I-III decreased to 6.55, 7.59, and 7.12 mg/L, lower than that in both 2D EKR and 3D GAC EKR. Besides, the leaching concentration in Sections VI and V after remediation decreased below the limiting values (5 mg/L) of leaching toxicity for hazardous wastes (GB5085.3-2007). The removal efficiency of Cr(VI) leaching was calculated and shown in **Table 4**. The rank of average removal efficiency of Cr(VI) leaching is 3D FeO_x/GAC (63.34%) > 2D (55.16%) > 3D-GAC (51.37%). This indicated the 3D FeO_x/GAC EKR was more capable of removing the Cr(VI) from soil and thus decrease the environmental risk resulting from hazardous Cr(VI) leaching.

$$H_2O \rightarrow \cdot OH + H^+ + e^- \quad (8)$$

Table 4. The removal efficiency of Cr leaching in experiment group B

Group B	Removal efficiency of Cr(VI) leaching (%)					Average
	I	II	III	IV	V	(%)
2D electrode	47.08	46.6	44.70	76.17	61.17	55.16
3D-GAC	45.82	42.98	46.96	62.81	58.25	51.37
3D-FeO_x/GAC	58.67	52.14	55.07	74.94	75.87	63.34

To further understand the Cr changes with time and space in the 3D FeO_x/GAC EKR system, the removal efficiency of Cr(VI) leaching and total Cr leaching after 7, 10, and 13 d was investigated (Fig 6(c)). It can be seen that the Cr leaching was dynamically influenced by the remediation time. The highest removal of Cr(VI) leaching in each test was obtained in Sections 7 d-IV (84.83%), 10 d-II (88.14%), and 13 d-I (88.97%); meanwhile, the lowest of that was obtained in Section 7 d-I (78.62%), 10 d-IV (75.72%) and 13 d-V (45.51%). This

implied that the accumulation position of soluble Cr(VI) moved from the near anode (e.g., Sections I and II) to the near cathode (e.g., Sections IV and V) with the increase of remediation time. Given that the near cathode sections were alkaline throughout the whole EKR process and Cr(VI) tends to migrate to the near anode area, the accumulation of Cr(VI) in the near cathode area in later remediation (10 - 13 d) was likely attributed to the oxidation of Cr(III).

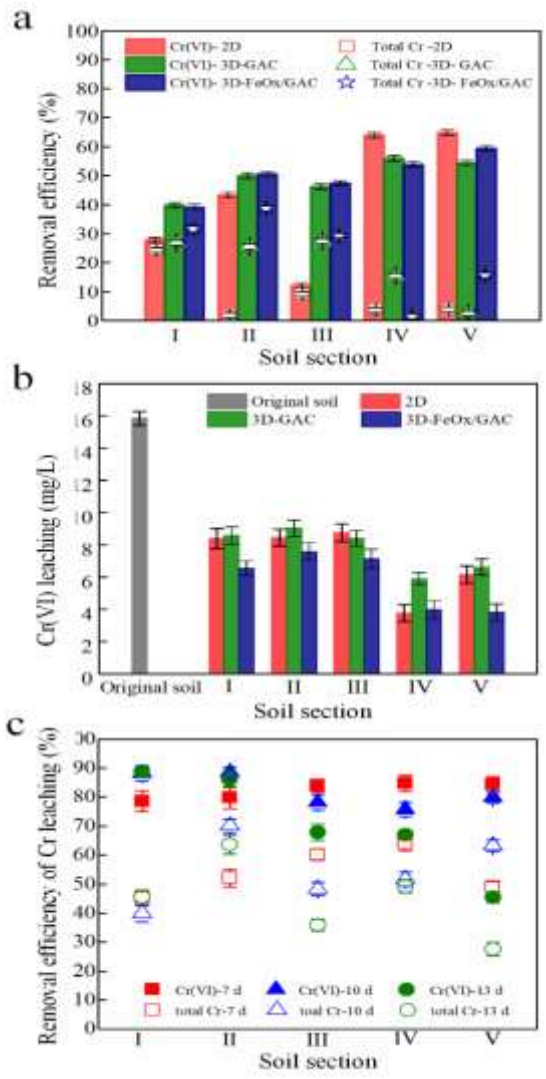

Fig. 7. (a) removal efficiency of Cr, (b) Cr(VI) leaching concentration, and (c) removal efficiency of Cr leaching after EKR.

3.5 Characteristics of FeO_x/GAC and soil before and after treatment

The morphology and elemental composition of FeO_x/GAC particles before and after EKR were examined by SEM-EDS, as shown in **Fig. 8a** and **8b**. The image of raw FeO_x/GAC (**Fig. 8a**) presented that iron oxide species with hexagonal lamellar shape was evenly dispersed on

the surface of GAC. After treatment, the surface structure was covered by substances mainly composed of C, O, Cr, Mg, Al, Ca, and Fe. The composition and crystal structure of raw FeO_x/GAC, used FeO_x/GAC-II, FeO_x/GAC-III, and FeO_x/GAC-IV exhibited significant differences in diffraction peaks (**Fig. 8c**). The two peaks of raw FeO_x/GAC, corresponding to carbon and iron oxides (**Fig. 4d**), disappeared after treatment. Instead, the FeO_x/GAC-II has three new main peaks at 26.8º, 29.5º, and 28.1º, attributed to the quartz SiO_2 (JCPDS card 46-1045), calcite $CaCO_3$ (JCPDS card 05-0586) and gismondine $CaAl_2Si_2O_8 \cdot 4H_2O$ (JCPDS card 20-0452). The crystalline phase of Cr was not observed, which indicated an amorphous form of Cr on the surface of FeO_x/GAC-II. The characteristic peak of gismondine disappeared on FeO_x/GAC-III; besides, new peaks at 26.4º and 36.2º was observed, in agreement with aragonite $CaCO_3$ (JCPDS card 41-1475). The aragonite is the polymorphism of calcite, which appears with a significant concentration of calcium ions and dissolved carbonate in the soil near FeO_x/GAC-III[62]. For FeO_x/GAC-IV, the aluminosilicate, i.e., anorthite $CaAl_2Si_2O_8$ (JCPDS card 41-1486), was also observed. Noticeably, a very stable Cr(III)-containing silicate (Uvarovite, $Ca_3Cr_2(SiO_4)_3$, JCPDS 11-0696) was observed and formed by the combination of Cr_2O_3, CaO, SiO_2, and a small amount of Al_2O_3. The other crystal phase of Cr(III)/Cr(VI) was not detected on used FeO_x/GAC, suggesting their presence as amorphous states or soluble ions, which may be attributed to the oxidation of Cr(III) by ·OH generated in E-Fenton reactions.

Fig. 8d shows the FTIR spectra of raw FeO_x/GAC, used FeO_x/GAC-II and FeO_x/GAC-IV. In the case of raw FeO_x/GAC, peaks at 3432, 3159, 1630, 1401, 1070, and 734 cm^{-1} correspond to the -OH stretching vibration, -CH stretching vibration, C=O vibration, C-C vibration, -COOH stretching vibration, and Fe-O stretching in Fe_2O_3/Fe_3O_4[63,64]. After EKR, the -CH functional group at 3159 cm^{-1} disappeared due to the complexation reaction between the amino group and Cr(VI). A new waveband at 467 cm^{-1} on both used particle electrodes was interpreted as the bending vibration of O-Si-O and Si-O-Si in the soil colloid. Besides, new peaks at 874 cm^{-1} of FeO_x/GAC-IV and 777 cm^{-1} of FeO_x/GAC-II represent the stretching vibration of Al-O or Si-O and bending vibration of Al-O-Si[65]. This result is related to the formation of aluminosilicates (e.g., anorthite) on the surface of the particle electrode. The intensity of the -

OH band enhanced especially on FeO_x/GAC-II, indicating the generation of hydroxyl radicals, which in turn interacted with Cr(VI) in a coordination reaction or participated in the oxidation of Cr(III). This is consistent with the XRD analysis. Generally, the oxidative/reductive reactions regarding Cr(VI)/Cr(III) can be interpreted by oxidation-reduction potential (ORP) in the soil. Considering it was hardly to measure ORP in the very small soil samples around the particle electrodes, the chemical states and corresponding relative proportions of Cr and Fe species in original soil, remediated soil and FeO_x/GAC particles were analyzed by XPS to investigate the interconversion between Cr(III) and Cr(VI), depicted in **Fig. 8e**. Compared to raw FeO_x/GAC, Fe 2p characteristic peak on FeO_x/GAC-II disappeared, indicating the substantial Fe loss on particle electrodes near the anode. Two new peaks at BE= 576 eV and 347.2 eV were detected on both FeO_x/GAC-II and FeO_x/GAC-III, recognized as the characteristic peaks of Cr 2p and Ca 2p, respectively. Spectral fitting and analysis of Cr $2p_{3/2}$ and Fe $2p_{3/2}$ data are summarized in **Table 5**. The valence state of both Cr and Fe with Cr $2p_{3/2}$ was only observed on FeO_x/GAC-III. Noticeably, the relative atomic proportion of Cr(VI) (23.4%) is higher than that of FeO_x/GAC-II (15.7%), while the relative atomic ratio of Fe(III) on FeO_x/GAC-III (61.0%) is higher than that on FeO_x/GAC-IV (27.3%). This means that on the surface of FeO_x/GAC-III, the Cr(VI) increased with increasing of Fe(III), indicating the occurrence of E-Fenton reactions and the oxidation of Cr(III), where ·OH free radicals were generated accompanied by consumption of Fe(II) and production of Fe(III), as shown in Eqs. (3) - (5).

Table 5. XPS binding energies of Cr 2p and Fe 2p core level on FeO_x/GAC-II, FeO_x/GAC-III, and FeO_x/GAC-IV with area and FWHM

Sample	Element	Spin orbit	Position(±0.1 eV)	FWHM (eV)	Chemical State	Area ratio
FeO_x/GAC-II	Cr	$2p_{3/2}$	579.2	1.44	Cr(VI)	0.15
			577.1	1.44	Cr(III)	
FeO_x/GAC-III	Cr	$2p_{3/2}$	579.1	2.26	Cr(VI)	0.23
			576.8	2.26	Cr(III)	
	Fe	$2p_{3/2}$	711.2	2.40	Fe(II)	0.61
			713.9	2.26	Fe(III)	
FeO_x/GAC-IV	Fe	$2p_{3/2}$	710.3	2.40	Fe(II)	0.27
			713.9	2.40	Fe(III)	

Further morphology and regional chemical composition of the soil before and after experiments were analyzed and shown in **Fig. 9**. It can be seen that the surface of the original soil particle was smooth and largely devoid of impurities, different from the ones from soil Sections II, III, and IV. A laminar structure was observed on both Sections III and IV, which might relate to the formation of calcium ions and magnesium ions bearing aluminosilicates in the soil. This was estimated by EDS analysis shown in **Fig. 9e**, which is consistent with XRD analysis of FeO_x/GAC-IV (e.g., anorthite and uvarovite) and a previous study which has reported a similar thin strip structure of quintinite-2H[66]. **Fig. 9f** illustrates the chemical valence and relative proportion of Cr on the used particle electrode, compared to its surrounding soil. Generally, the valence state proportion of Cr on the surface of particle electrodes is not much different from that in its surrounding soil. Whereas, according to peak fitting results of Cr $2p_{3/2}$, the relative proportions of Cr(VI) and Cr(III) compounds on FeO_x/GAC-II were 25.41% and 74.59%, while that on its surrounding soil were 14.56% and 85.44%. This implied the minor reduction of Cr(VI) on the surface of particle electrodes in near anode sections. In the case of soil Section IV, the Cr(VI) proportion on particle electrodes increased to 45.30% compared to 18.57% in ambient soil. This suggested a considerable transformation of Cr(III) to Cr(VI) on particle electrodes.

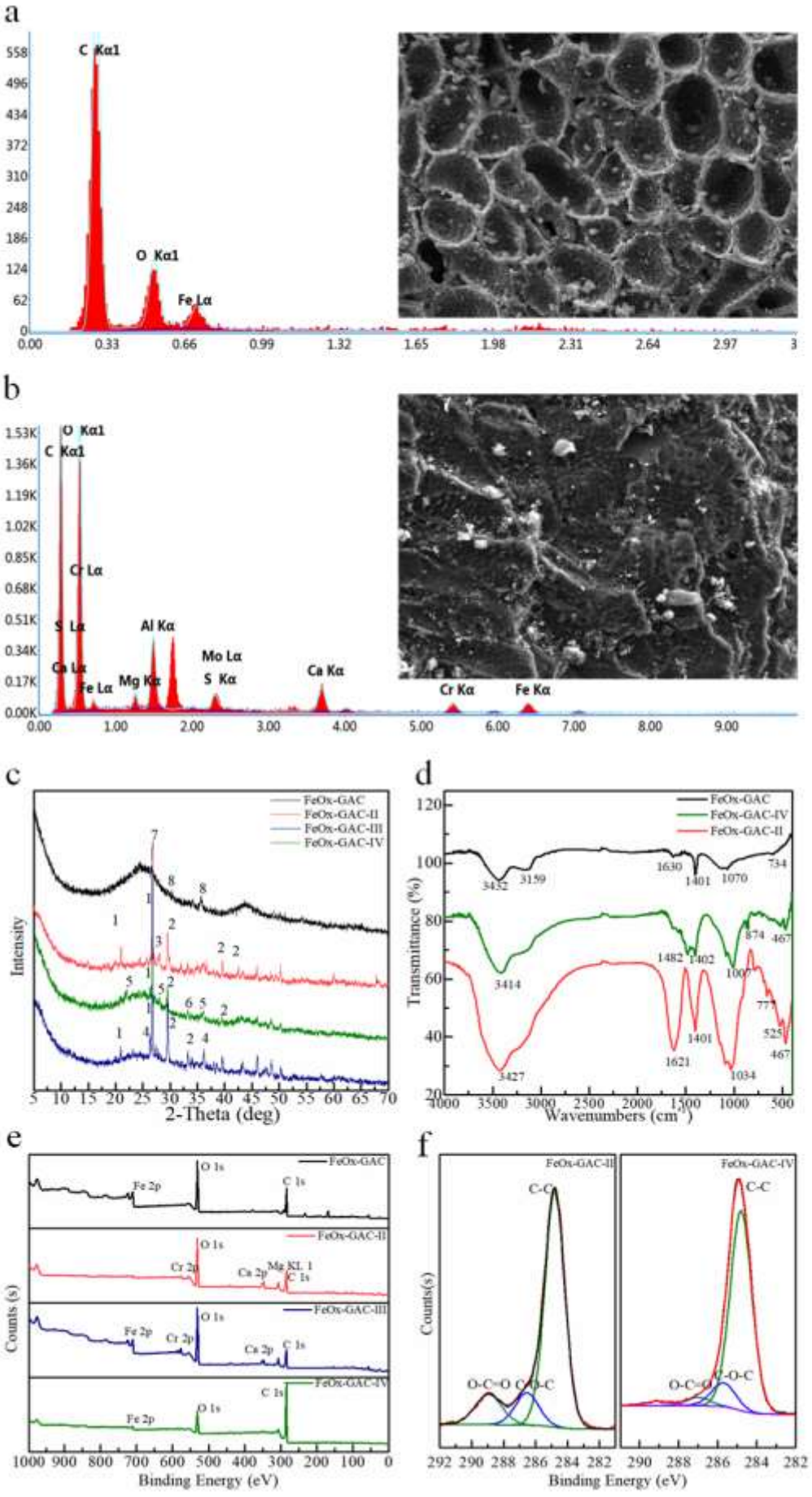
a
C Kα1
O Kα1
Fe Lα
b
O Kα1
C Kα1
Cr Lα
S Lα
Al Kα
Mo Lα
S Kα
Ca Kα
Ca Lα
Fe Lα
Mg Kα
Cr Kα
Fe Kα
c
FeOx-GAC
FeOx-GAC-II
FeOx-GAC-III
FeOx-GAC-IV
Intensity
2-Theta (deg)
d
FeOx-GAC
FeOx-GAC-IV
FeOx-GAC-II
Transmittance (%)
Wavenumbers (cm-1)
3432
3159
1630
1401
1070
734
3414
1482
1402
1007
874
467
777
525
3427
1621
1401
1034
e
FeOx-GAC
FeOx-GAC-II
FeOx-GAC-III
FeOx-GAC-IV
O 1s
C 1s
Fe 2p
Cr 2p
Ca 2p
Mg KL 1
Counts (s)
Binding Energy (eV)
f
FeOx-GAC-II
FeOx-GAC-IV
C-C
O-C=O
C-O-C
Counts(s)
Binding Energy (eV)

522

Fig. 8 SEM images and EDS spectra of FeO_x/GAC (a) before and (b) after treatment; (c) XRD pattern, (d) FTIR spectra, (e) XPS survey of raw and used FeO_x/GAC, and (f) C 1s peak fitting spectra.

1: Quartz, syn, SiO_2; 2: Calcite, $CaCO_3$; 3: Gismondine, $CaAl_2Si_2O_8 \cdot 4H_2O$; 4: Aragonite, $CaCO_3$; 5: Anorthite, ordered, $CaAl_2Si_2O_8$; 6: Uvarovite,syn, $Ca_3Cr_2(SiO_4)_3$; 7: Carbon, C; 8: Maghemite, syn, Fe_2O_3 or Magnetite, syn, Fe_3O_4.

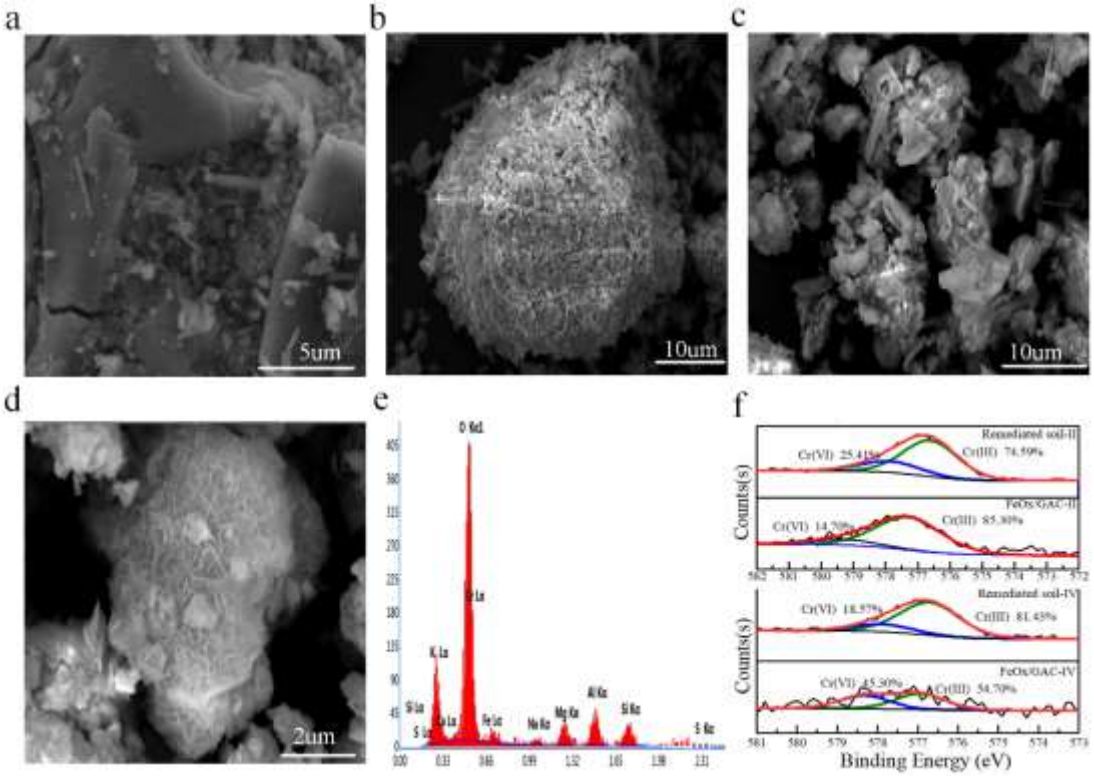

Fig. 9 SEM images of (a) original soil, treated soil from (b) Section II, (c) Section (III) and (d)Section (VI); (e) EDS spectrum for treated soil section IV, and (f) Cr $2p_{3/2}$ spectra of used FeO_x/GAC and ambient treated soil.

534 3.6 Migration and transformation of Cr in FeO_x/GAC-based 3D EKR system

535 Cr migration under EKR depends upon a wide range of electrochemical factors, including
536 pH and redox reactions which in turn have a direct influence on Cr transformation processes
537 such as adsorption/electrosorption, desorption, precipitation, and dissolution. The non-
538 uniformity of pH and Eh typically recorded in 2D EKR systems leads to the development of a
539 wide range of such Cr immobilization processes. In contrast the presence of a third electrode
540 (i.e. as an array of third electrodes disseminated throughout the soil matrix) has the potential to
541 circumvent such unwanted phenomena.

542 According to the resulted collected herein, the initial stage of the FeO_x/GAC- based 3D
543 EKR system, comprised the movement of water-soluble Cr(VI) (present in the original soil
544 sample), likely in the form of oxygen anions (e.g., $Cr_2O_7^{2-}$ and $HCr_2O_7^-$), into the anolyte via
545 electromigration. Such an electromigration process is the root cause of Cr(VI) removal from
546 soil and occurs continuously under the action of the electric field. Meanwhile, H^+ and OH^-,
547 generated on the counter electrodes, entered the soil (which was still alkaline, with any Cr(III)
548 therefore in a precipitated phase). FeO_x/GAC also underwent polarization to form a miniature
549 electrolytic cell, where adsorption/electrosorption and hydrolysis reactions on the particle
550 electrode occurred. Within this process, potential reactions occurred: ferrous ions released from
551 FeO_x reduced Cr(VI) to Cr(III) and subsequently either co-precipitated with Cr(III) or migrated
552 towards the cathode, depending on soil pH conditions, according to the electrochemical
553 reactions shown in Eqs. (9) - (11):

554 $$Fe_3O_4 + 8H^+ \rightarrow Fe^{2+} + 2Fe^{3+} + 4H_2O \quad (9)$$

555 $$Cr_2O_7{}^{2-} + 6Fe^{2+} + 14H^+ + GAC \rightarrow 2Cr^{3+} + 6Fe^{3+} + 7H_2O + GAC \quad (10)$$

556 $$(1 - Y)Fe^{3+} + YCr^{3+} + 3OH^- \rightarrow Fe_{1-Y}Cr_Y(OH)_3 \quad (11)$$

557 As reactions progressed, a soil acidification front was developed in the soil adjacent to the
558 anode. Cr(III), which was likely bound to carbonates and hydroxide precipitate phases, in near
559 anode soil were therefore released and underwent electromigration towards the cathode.
560 Precipitation then likely occurred in proximity to the cathode when encountering the elevated

pH conditions. In such locations where the pH increase was significant (pH>11), chromium hydroxide precipitates also likely dissolved, forming $Cr(OH)_4^-$[67], and therefore were attracted towards the anode, as shown in Eq. (12).

$$Cr(OH)_3 + OH^- \rightarrow Cr(OH)_4^- \quad (12)$$

The presence of FeO_x/GAC enables the superimposition of E-Fenton reactions (Eqs. (3) and (4)) onto such processes, where strong oxidizing hydroxyl radicals were produced and released into the soil to promote the oxidation of Cr(III) to highly mobile Cr(VI) and consequently enable greater Cr movement to the anode via electromigration. Moreover in proximity to the cathode the presence of such FeO_x/GAC also likely facilitates the greater conversion of Cr(III) to stable silicates, therefore decreasing the mobility of any residual Cr within the soil. And thus the toxicity of Cr-contaminated soil was reduced significantly.

4. Conclusion

This study has reported, for the first time, the application of a novel 3D EKR system for the removal of Cr from a real contaminated soil sample. Whilst many studies have investigated the application of 2D EKR for the removal of Cr from different matrices. Major technical challenges remain due to a range of factors including ineffective aqueous Cr removal and the tendency of Cr to undergo precipitation as partially soluble precipitate phases, which therefore are amenable for remobilization in the future. Herein we have compared the efficacy of both 2D and 3D (with FeO_x/GAC composite particles comprising the third electrodes) EKR systems for the remediation of Cr from a real contaminated soil.

Overall our results suggest that 3D EKR enables higher total Cr removal efficiency and lower leaching concentration than 2D EKR. The maximum removal of Cr(VI) leaching reached 88.9% after 13 d remediation. The presence of FeO_x/GAC particle electrodes was capable of not only alleviating the acid-base polarization in soil resulting from hydrolysis of main electrodes but also creating a higher and more stable current density in the 3D EKR system by functioning as current carriers, which facilitated the electromigration of both Cr(VI) and Cr(III). The 3D EKR also enabled the oxidation of Cr(III) to Cr(VI) on FeO_x/GAC in the near cathode soil region (recorded using XPS and Cr(VI) leaching data) which further facilitated its removal

from the soil via electromigration, due to the greater solubility of Cr(VI). In regions in proximity to the cathode the transformation of Cr(III) to stable silicates was also promoted, which due to their low solubility, also further lowered the toxicity of the contaminated soil.

This study therefore provides a highly promising first proof of concept for this new approach to Cr remediation from soil. Future work is required in order to further understand the fundamental electrochemical mechanisms explored herein in both different soil and contaminant systems but also at greater scale and for longer time periods. Within this the major steps forward would be the direct measurement and associated numerical modelling of hydroxyl radical formation on soil regions adjacent to particles electrodes and the energy consumption in the 3D EKR process. Such research would provide further validation of this new contaminated land remediation process and thereby accelerate its development towards potential future commercial applications.

Acknowledgment

This study was financially supported by the Natural Science Foundation of Anhui University of Technology (QZ202110) and Research funds of Engineering Research Center of Biofilm Water Purification and Utilization Technology, Ministry of Education (BWPU2020KF05). We also acknowledge support from the UK Natural Environment Research Council (NE/W006820/1).

References

(1) Li, H.; Yang, Y.; Zheng, W.; Chen, L.; Bai, Y. Immobilization of High Concentration Hexavalent Chromium via Core-Shell Structured Lightweight Aggregate: A Promising Soil Remediation Strategy. *Chemical Engineering Journal* **2020**, *401*, 126044. https://doi.org/10.1016/J.CEJ.2020.126044.

(2) Fan, C.; Qian, J.; Yang, Y.; Sun, H.; Song, J.; Fan, Y. Green Ceramsite Production via Calcination of Chromium Contaminated Soil and the Toxic Cr(VI) Immobilization Mechanisms. *J Clean Prod* **2021**, *315*, 128204. https://doi.org/10.1016/J.JCLEPRO.2021.128204.

(3) Huang, T.; Liu, L.; Zhou, L.; Zhang, S. Electrokinetic Removal of Chromium from Chromite Ore-Processing Residue Using Graphite Particle-Supported Nanoscale Zero-Valent Iron as the Three-Dimensional Electrode. *Chemical Engineering Journal* **2018**, *350*, 1022–1034. https://doi.org/10.1016/j.cej.2018.06.048.

(4) Dhal, B.; Thatoi, H. N.; Das, N. N.; Pandey, B. D. Chemical and Microbial Remediation of Hexavalent Chromium from Contaminated Soil and Mining/Metallurgical Solid Waste: A Review. *J Hazard Mater* **2013**, *250–251*, 272–291. https://doi.org/10.1016/J.JHAZMAT.2013.01.048.

(5) Su, H.; Fang, Z.; Tsang, P. E.; Fang, J.; Zhao, D. Stabilisation of Nanoscale Zero-Valent Iron with Biochar for Enhanced Transport and in-Situ Remediation of Hexavalent Chromium in Soil. *Environmental Pollution* **2016**, *214*, 94–100. https://doi.org/10.1016/J.ENVPOL.2016.03.072.

(6) Eyvazi, B.; Jamshidi-Zanjani, A.; Khodadadi Darban, A. Immobilization of Hexavalent Chromium in Contaminated Soil Using Nano-Magnetic MnFe2O4. *J Hazard Mater* **2019**, *365*, 813–819. https://doi.org/10.1016/J.JHAZMAT.2018.11.041.

(7) Ali, S.; Bai, P.; Zeng, F.; Cai, S.; Shamsi, I. H.; Qiu, B.; Wu, F.; Zhang, G. The Ecotoxicological and Interactive Effects of Chromium and Aluminum on Growth, Oxidative Damage and Antioxidant Enzymes on Two Barley Genotypes Differing in Al Tolerance. *Environ Exp Bot* **2011**, *70* (2–3), 185–191. https://doi.org/10.1016/J.ENVEXPBOT.2010.09.002.

(8) DesMarias, T. L.; Costa, M. Mechanisms of Chromium-Induced Toxicity. *Curr Opin Toxicol* **2019**, *14*, 1–7. https://doi.org/10.1016/J.COTOX.2019.05.003.

(9) Sung, M.; Lee, C. Y.; Lee, S. Z. Combined Mild Soil Washing and Compost-Assisted Phytoremediation in Treatment of Silt Loams Contaminated with Copper, Nickel, and Chromium. *J Hazard Mater* **2011**, *190* (1–3), 744–754. https://doi.org/10.1016/J.JHAZMAT.2011.03.113.

(10) Sun, Y.; Guan, F.; Yang, W.; Wang, F. Removal of Chromium from a Contaminated Soil Using Oxalic Acid, Citric Acid, and Hydrochloric Acid: Dynamics, Mechanisms, and Concomitant Removal of Non-Targeted Metals. *International Journal of Environmental Research and Public Health 2019, Vol. 16, Page 2771* **2019**, *16* (15), 2771. https://doi.org/10.3390/IJERPH16152771.

(11) Dermont, G.; Bergeron, M.; Mercier, G.; Richer-Laflèche, M. Soil Washing for Metal Removal: A Review of Physical/Chemical Technologies and Field Applications. *J Hazard Mater* **2008**, *152* (1), 1–31. https://doi.org/10.1016/J.JHAZMAT.2007.10.043.

(12) Wang, J.; Liu, X.; Zhu, Z.; Yuan, L.; Zhao, D.; Deng, H.; Lin, Z. Microwave-Enhanced Reductive Immobilization of High Concentrations of Chromium in a Field Soil Using Iron Polysulfide. *J Hazard Mater* **2021**, *418*, 126293. https://doi.org/https://doi.org/10.1016/j.jhazmat.2021.126293.

(13) Shah, V.; Daverey, A. Phytoremediation: A Multidisciplinary Approach to Clean up Heavy Metal Contaminated Soil. *Environ Technol Innov* **2020**, *18*, 100774. https://doi.org/https://doi.org/10.1016/j.eti.2020.100774.

(14) Palansooriya, K. N.; Shaheen, S. M.; Chen, S. S.; Tsang, D. C. W.; Hashimoto, Y.; Hou, D.; Bolan, N. S.; Rinklebe, J.; Ok, Y. S. Soil Amendments for Immobilization of Potentially Toxic Elements in Contaminated Soils: A Critical Review. *Environ Int* **2020**, *134*, 105046. https://doi.org/https://doi.org/10.1016/j.envint.2019.105046.

(15) Zhang, H.; Yuan, X.; Xiong, T.; Wang, H.; Jiang, L. Bioremediation of Co-Contaminated Soil with Heavy Metals and Pesticides: Influence Factors, Mechanisms and Evaluation Methods. *Chemical Engineering Journal* **2020**, *398*, 125657. https://doi.org/https://doi.org/10.1016/j.cej.2020.125657.

(16) Jeon, E.-K.; Ryu, S.-R.; Baek, K. Application of Solar-Cells in the Electrokinetic Remediation of As-Contaminated Soil. *Electrochim Acta* **2015**, *181*, 160–166. https://doi.org/https://doi.org/10.1016/j.electacta.2015.03.065.

(17) Hahladakis, J. N.; Latsos, A.; Gidarakos, E. Performance of Electroremediation in Real Contaminated Sediments Using a Big Cell,

Periodic Voltage and Innovative Surfactants. *J Hazard Mater* **2016**, *320*, 376–385. https://doi.org/https://doi.org/10.1016/j.jhazmat.2016.08.003.

(18) Wen, D.; Fu, R.; Li, Q. Removal of Inorganic Contaminants in Soil by Electrokinetic Remediation Technologies: A Review. *J Hazard Mater* **2021**, *401*, 123345. https://doi.org/10.1016/J.JHAZMAT.2020.123345.

(19) Robles, I.; Lozano, M. J.; Solís, S.; Hernández, G.; Paz, M. V; Olvera, M. G.; Bustos, E. Electrokinetic Treatment Of Mercury-Polluted Soil Facilitated By Ethylenediaminetetraacetic Acid Coupled With A Reactor With A Permeable Reactive Barrier Of Iron To Recover Mercury (II) From Water. *Electrochim Acta* **2015**, *181*, 68–72. https://doi.org/https://doi.org/10.1016/j.electacta.2015.04.099.

(20) Sawada, A.; Mori, K. I.; Tanaka, S.; Fukushima, M.; Tatsumi, K. Removal of Cr(VI) from Contaminated Soil by Electrokinetic Remediation. *Waste Management* **2004**, *24* (5), 483–490. https://doi.org/10.1016/S0956-053X(03)00133-8.

(21) Sun, T. R.; Pamukcu, S.; Ottosen, L. M.; Wang, F. Electrochemically Enhanced Reduction of Hexavalent Chromium in Contaminated Clay: Kinetics, Energy Consumption, and Application of Pulse Current. *Chemical Engineering Journal* **2015**, *262*, 1099–1107. https://doi.org/10.1016/J.CEJ.2014.10.081.

(22) Tang, J.; He, J.; Liu, T.; Xin, X.; Hu, H. Removal of Heavy Metal from Sludge by the Combined Application of a Biodegradable Biosurfactant and Complexing Agent in Enhanced Electrokinetic Treatment. *Chemosphere* **2017**, *189*, 599–608. https://doi.org/https://doi.org/10.1016/j.chemosphere.2017.09.104.

(23) Lehoux, A. P.; Sanchez-Hachair, A.; Lefebvre, G.; Carlier, G.; Hébrard, C.; Lima, A. T.; Hofmann, A. Chromium (VI) Retrieval from Chromium Ore Processing Residues by Electrokinetic Treatment. *Water Air Soil Pollut* **2017**, *228* (9), 378. https://doi.org/10.1007/s11270-017-3562-7.

(24) Gonzini, O.; Plaza, A.; Di Palma, L.; Lobo, M. C. Electrokinetic Remediation of Gasoil Contaminated Soil Enhanced by Rhamnolipid. *J Appl Electrochem* **2010**, *40* (6), 1239–1248. https://doi.org/10.1007/s10800-010-0095-9.

(25) Li, S.; Li, T.; Li, G.; Li, F.; Guo, S. Enhanced Electrokinetic Remediation of Chromium-Contaminated Soil Using Approaching Anodes. *Front Environ Sci Eng* **2012**, *6* (6), 869–874. https://doi.org/10.1007/s11783-012-0437-4.

(26) Lee, H.-H.; Yang, J.-W. A New Method to Control Electrolytes PH by Circulation System in Electrokinetic Soil Remediation. *J Hazard Mater* **2000**, *77* (1), 227–240. https://doi.org/https://doi.org/10.1016/S0304-3894(00)00251-X.

(27) Ma, Y.; Li, X.; Mao, H.; Wang, B.; Wang, P. Remediation of Hydrocarbon–Heavy Metal Co-Contaminated Soil by Electrokinetics Combined with Biostimulation. *Chemical Engineering Journal* **2018**, *353*, 410–418. https://doi.org/https://doi.org/10.1016/j.cej.2018.07.131.

(28) Yan, Y.; Li, H.; Yu, X.; Li, S.; Huang, X.; Li, D.; Jiao, B. Efficient Removal of Chromium from Soil in a Modified Electrokinetic System Using Iron-Treated Activated Carbon as Third Electrode. *J Taiwan Inst Chem Eng* **2019**, *101*, 15–23. https://doi.org/10.1016/j.jtice.2019.03.021.

(29) Zhang, C.; Jiang, Y.; Li, Y.; Hu, Z.; Zhou, L.; Zhou, M. Three-Dimensional Electrochemical Process for Wastewater Treatment: A General Review. *Chemical Engineering Journal* **2013**, *228*, 455–467. https://doi.org/10.1016/J.CEJ.2013.05.033.

(30) Pamukcu, S.; Weeks, A.; Wittle, J. K. Enhanced Reduction of Cr(VI) by Direct Electric Current in a Contaminated Clay. *Environ Sci Technol* **2004**, *38* (4), 1236–1241. https://doi.org/10.1021/es034578v.

(31) Mukhopadhyay, B.; Sundquist, J.; Schmitz, R. J. Removal of Cr(VI) from Cr-

Contaminated Groundwater through Electrochemical Addition of Fe(II). *J Environ Manage* **2007**, *82* (1), 66–76. https://doi.org/https://doi.org/10.1016/j.jenvman.2005.12.005.

(32) Weng, C.-H.; Lin, Y.-T.; Lin, T. Y.; Kao, C. M. Enhancement of Electrokinetic Remediation of Hyper-Cr(VI) Contaminated Clay by Zero-Valent Iron. *J Hazard Mater* **2007**, *149* (2), 292–302. https://doi.org/https://doi.org/10.1016/j.jhazmat.2007.03.076.

(33) Stepniewska, Z.; Bucior, K.; Bennicelli, R. P. The Effects of MnO2 on Sorption and Oxidation of Cr(III) by Soils. *Geoderma* **2004**, *122* (2–4), 291–296. https://doi.org/10.1016/J.GEODERMA.2004.01.015.

(34) Xu, T.; Jiang, X.; Tang, Y.; Zeng, Y.; Zhang, W.; Shi, B. Oxidation of Trivalent Chromium Induced by Unsaturated Oils: A Pathway for Hexavalent Chromium Formation in Soil. *J Hazard Mater* **2021**, *405*, 124699. https://doi.org/10.1016/J.JHAZMAT.2020.124699.

(35) Bakker, M. G.; Fowler, B.; Bowman, M. K.; Patience, G. S. Experimental Methods in Chemical Engineering: Electron Paramagnetic Resonance Spectroscopy-EPR/ESR. *Can J Chem Eng* **2020**, *98* (8), 1668–1681. https://doi.org/10.1002/CJCE.23784.

(36) Wang, L.; Lan, X.; Peng, W.; Wang, Z. Uncertainty and Misinterpretation over Identification, Quantification and Transformation of Reactive Species Generated in Catalytic Oxidation Processes: A Review. *J Hazard Mater* **2021**, *408*, 124436. https://doi.org/10.1016/J.JHAZMAT.2020.124436.

(37) Xie, J.; Zhang, C.; Waite, T. D. Hydroxyl Radicals in Anodic Oxidation Systems: Generation, Identification and Quantification. *Water Res* **2022**, *217*, 118425. https://doi.org/10.1016/J.WATRES.2022.118425.

(38) Nakabayashi, Y.; Nosaka, Y. OH Radical Formation at Distinct Faces of Rutile TiO2 Crystal in the Procedure of Photoelectrochemical Water Oxidation. *Journal of Physical Chemistry C* **2013**, *117* (45), 23832–23839. https://doi.org/10.1021/JP408244H.

(39) Jung, K. H.; Zhang, X. Fluorogenic Detection of Protein Aggregates in Live Cells Using the AggTag Method. *Methods Enzymol* **2020**, *639*, 1–22. https://doi.org/10.1016/BS.MIE.2020.04.006.

(40) Zhu, X.; Ni, J.; Xing, X.; Li, H.; Jiang, Y. Synergies between Electrochemical Oxidation and Activated Carbon Adsorption in Three-Dimensional Boron-Doped Diamond Anode System. *Electrochim Acta* **2011**, *56* (3), 1270–1274. https://doi.org/https://doi.org/10.1016/j.electacta.2010.10.073.

(41) Kohantorabi, M.; Moussavi, G.; Giannakis, S. A Review of the Innovations in Metal- and Carbon-Based Catalysts Explored for Heterogeneous Peroxymonosulfate (PMS) Activation, with Focus on Radical vs. Non-Radical Degradation Pathways of Organic Contaminants. *Chemical Engineering Journal* **2021**, *411*, 127957. https://doi.org/https://doi.org/10.1016/j.cej.2020.127957.

(42) Mariana, M.; H.P.S., A. K.; Mistar, E. M.; Yahya, E. B.; Alfatah, T.; Danish, M.; Amayreh, M. Recent Advances in Activated Carbon Modification Techniques for Enhanced Heavy Metal Adsorption. *Journal of Water Process Engineering* **2021**, *43*, 102221. https://doi.org/https://doi.org/10.1016/j.jwpe.2021.102221.

(43) Marghaki, N. S.; Jonoush, Z. A.; Rezaee, A. Improving the Performance of Cr (VI) Removal by Electrochemical Process Using Microbial Cellulose/Magnetic Nanoparticles Electrode. *J Clean Prod* **2020**, *277*, 123195. https://doi.org/10.1016/J.JCLEPRO.2020.123195.

(44) Marghaki, N. S.; Jonoush, Z. A.; Rezaee, A. Chromium (VI) Removal Using Microbial Cellulose/ Nano-Fe3O4 @polypyrrole: Isotherm, Kinetic and Thermodynamic Studies. *Mater Chem Phys* **2022**, *278*, 125696.

https://doi.org/10.1016/J.MATCHEMPHYS.2022.125696.
(45) Tian, X.; Liu, M.; Iqbal, K.; Ye, W.; Chang, Y. Facile Synthesis of Nitrogen-Doped Carbon Coated Fe3O4/Pd Nanoparticles as a High-Performance Catalyst for Cr (VI) Reduction. *J Alloys Compd* **2020**, *826*, 154059. https://doi.org/10.1016/J.JALLCOM.2020.154059.
(46) Zhao, H.; Wang, Y.; Wang, Y.; Cao, T.; Zhao, G. Electro-Fenton Oxidation of Pesticides with a Novel Fe3O4@Fe2O3/Activated Carbon Aerogel Cathode: High Activity, Wide PH Range and Catalytic Mechanism. *Appl Catal B* **2012**, *125*, 120–127. https://doi.org/10.1016/J.APCATB.2012.05.044.
(47) Li, D.; Yu, J.; Jia, J.; He, H.; Shi, W.; Zheng, T.; Ma, J. Coupling Electrode Aeration and Hydroxylamine for the Enhanced Electro-Fenton Degradation of Organic Contaminant: Improving H2O2 Generation, Fe3+/Fe2+ Cycle and N2 Selectivity. *Water Res* **2022**, *214*, 118167. https://doi.org/10.1016/J.WATRES.2022.118167.
(48) Wu, J.; Zhao, Y.; Li, K.; Muhammad, S.; Ju, M.; Liu, L.; Huang, Y.; Wang, B.; Ding, W.; Shen, B.; Huang, H. Fluorogenic Toolbox for Facile Detecting of Hydroxyl Radicals: From Designing Principles to Diagnostics Applications. *TrAC - Trends in Analytical Chemistry* **2022**, *157*. https://doi.org/10.1016/J.TRAC.2022.116734.
(49) Yan, Y.; Xue, F.; Muhammad, F.; Yu, L.; Xu, F.; Jiao, B.; Shiau, Y. C.; Li, D. Application of Iron-Loaded Activated Carbon Electrodes for Electrokinetic Remediation of Chromium-Contaminated Soil in a Three-Dimensional Electrode System. *Sci Rep* **2018**, *8* (1), 1–11. https://doi.org/10.1038/s41598-018-24138-z.
(50) Sumner, M. E.; Miller, W. P. Cation Exchange Capacity and Exchange Coefficients. *undefined* **2018**, 1201–1229. https://doi.org/10.2136/SSSABOOKSER5.3.C40.
(51) Li, J.; Yan, J.; Yao, G.; Zhang, Y.; Li, X.; Lai, B. Improving the Degradation of Atrazine in the Three-Dimensional (3D) Electrochemical Process Using CuFe2O4 as Both Particle Electrode and Catalyst for Persulfate Activation. *Chemical Engineering Journal* **2019**, *361*, 1317–1332. https://doi.org/https://doi.org/10.1016/j.cej.2018.12.144.
(52) Zhan, M. X.; Liu, Y. W.; Ye, W. W.; Chen, T.; Jiao, W. T. Modification of Activated Carbon Using Urea to Enhance the Adsorption of Dioxins. *Environ Res* **2022**, *204*, 112035. https://doi.org/10.1016/J.ENVRES.2021.112035.
(53) Banerjee, S.; Banerjee, I.; Dutta, M.; Pal, R. Fabrication of Iron Nanoparticles Using Leptolyngbya Valderiana and Investigation of Its Cr (VI) Removal Potential in the Free and Biomass Associated Forms. *Algal Res* **2021**, *58*, 102373. https://doi.org/10.1016/J.ALGAL.2021.102373.
(54) Zhang, L.; Dong:, Y.; Liu, J.; Liu, W.; Lu, Y.; Lin, H. Promotion of Higher Synthesis Temperature for Higher-Efficient Removal of Antimonite and Antimonate in Aqueous Solution by Iron-Loaded Porous Biochar. *Bioresour Technol* **2022**, *363*, 127889. https://doi.org/10.1016/J.BIORTECH.2022.127889.
(55) Wang, X.; Wu, L.; Wang, J.; Zhou, Y.; Wang, Y.; Wu, W. D.; Li, W.; Wu, Z. Oxygen Vacancies and Interfacial Iron Sites in Hierarchical BiOCl Nanosheet Microflowers Cooperatively Promoting Photo-Fenton. *Chemosphere* **2022**, *307*, 135967. https://doi.org/10.1016/J.CHEMOSPHERE.2022.135967.
(56) Lu, P.; Feng, Q.; Meng, Q.; Yuan, T. Electrokinetic Remediation of Chromium- and Cadmium-Contaminated Soil from Abandoned Industrial Site. *Sep Purif Technol* **2012**, *98*, 216–220. https://doi.org/10.1016/j.seppur.2012.07.010.
(57) Suzuki, T.; Kawai, K.; Moribe, M.; Niinae, M. Recovery of Cr as Cr(III) from Cr(VI)-Contaminated Kaolinite Clay by Electrokinetics Coupled with a

Permeable Reactive Barrier. *J Hazard Mater* **2014**, *278*, 297–303. https://doi.org/10.1016/J.JHAZMAT.2014.05.086.

(58) Yan, Y.; Kirkelund, G. M. Graphite Particles as Third Electrodes to Enhance Metal Removal and Energy Saving in a Stationary Electrodialytic Soil System. *Electrochim Acta* **2022**, *407*, 139896. https://doi.org/10.1016/j.electacta.2022.139896.

(59) Wang, Y.; Huang, L.; Wang, Z.; Wang, L.; Han, Y.; Liu, X.; Ma, T. Application of Polypyrrole Flexible Electrode for Electrokinetic Remediation of Cr(VI)-Contaminated Soil in a Main-Auxiliary Electrode System. *Chemical Engineering Journal* **2019**, *373*, 131–139. https://doi.org/10.1016/J.CEJ.2019.05.016.

(60) Li, D.; Xiong, Z.; Nie, Y.; Niu, Y. Y.; Wang, L.; Liu, Y. Y. Near-Anode Focusing Phenomenon Caused by the High Anolyte Concentration in the Electrokinetic Remediation of Chromium(VI)-Contaminated Soil. *J Hazard Mater* **2012**, *229–230*, 282–291. https://doi.org/10.1016/J.JHAZMAT.2012.05.107.

(61) Wu, J.; Zhang, J.; Xiao, C. Focus on Factors Affecting PH, Flow of Cr and Transformation between Cr(VI) and Cr(III) in the Soil with Different Electrolytes. *Electrochim Acta* **2016**, *211*, 652–662. https://doi.org/10.1016/J.ELECTACTA.2016.06.048.

(62) Li, Y.; Liu, W.; Xing, F.; Wang, S.; Tang, L.; Lin, S.; Dong, Z. Carbonation of the Synthetic Calcium Silicate Hydrate (C-S-H) under Different Concentrations of CO2: Chemical Phases Analysis and Kinetics. *Journal of CO2 Utilization* **2020**, *35*, 303–313. https://doi.org/https://doi.org/10.1016/j.jcou.2019.10.001.

(63) Li, G.; Guo, S.; Li, S.; Zhang, L.; Wang, S. Comparison of Approaching and Fixed Anodes for Avoiding the 'Focusing' Effect during Electrokinetic Remediation of Chromium-Contaminated Soil. *Chemical Engineering Journal* **2012**, *203*, 231–238. https://doi.org/10.1016/J.CEJ.2012.07.008.

(64) Wang, Y.; Fang, Z.; Liang, B.; Tsang, E. P. Remediation of Hexavalent Chromium Contaminated Soil by Stabilized Nanoscale Zero-Valent Iron Prepared from Steel Pickling Waste Liquor. *Chemical Engineering Journal* **2014**, *247*, 283–290. https://doi.org/10.1016/J.CEJ.2014.03.011.

(65) Tian, Q.; Bai, Y.; Pan, Y.; Yao, S.; Chen, C.; Zhang, H.; Sasaki, K. Influence of Aluminate and Silicate on Selenate Immobilization Using Alkaline-Earth Metal Oxides and Ferrous Salt. *Science of The Total Environment* **2022**, *851*, 158126. https://doi.org/10.1016/J.SCITOTENV.2022.158126.

(66) Yan, Y.; Li, H.; Yu, X.; Li, S.; Huang, X.; Li, D.; Jiao, B. Efficient Removal of Chromium from Soil in a Modified Electrokinetic System Using Iron-Treated Activated Carbon as Third Electrode. *J Taiwan Inst Chem Eng* **2019**, *101*, 15–23.

(67) Unceta, N.; Séby, F.; Malherbe, J.; Donard, O. F. X. Chromium Speciation in Solid Matrices and Regulation: A Review. *Anal Bioanal Chem* **2010**, *397* (3), 1097–1111. https://doi.org/10.1007/S00216-009-3417-1/TABLES/8.